



The 1956 Greek tsunami recorded at Yafo, Israel, and its numerical modeling

S. Beisel,¹ L. Chubarov,¹ I. Didenkulova,² E. Kit,^{3,4} A. Levin,⁵ E. Pelinovsky,⁶ Y. Shokin,¹ and M. Sladkevich⁵

Received 31 December 2008; revised 20 May 2009; accepted 12 June 2009; published 1 September 2009.

[1] A record of a tsunami event riding on the usual tide signal was recorded by a floating-type tidal gauge installed in the port of Yafo, Israel. The tsunami was triggered by an earthquake in the Aegean Sea on 9 July 1956. This paper presents a retrieval of tsunami waves from the record. At the first stage of the study an attempt had been undertaken to reproduce the 1956 tsunami assuming a coseismic nature of its generation source. Although these simulations resulted in tsunami waves with their amplitude close to that obtained from the record measured at Yafo, they did not contain significant spectral energy components with periods of ~ 15 min as appear in the spectra of 1956 tide-gauge records. When landslide movement, triggered by the main shock and/or by the largest aftershock, is suggested as a source of these tsunami waves, the spectra of the resulted marigram obtained in the proximity to Yafo contain harmonics with frequencies very close to those measured. This corroborates the landslide nature of the tsunamigenic source responsible for generation of higher-frequency (relative to the tidal waves) energy components. The peak periods determined via spectral analysis of the recent tide-gauge records (1 year and longer) in the absence of tsunami events vary from 50 to 60 min. Similar periods have been revealed in a special numerical study dealing with longwave propagation toward the coast of Israel, thus confirming that their origin is related to continental shelf resonance. These resonance periods differ significantly from those found for the 1956 tsunami.

Citation: Beisel, S., L. Chubarov, I. Didenkulova, E. Kit, A. Levin, E. Pelinovsky, Y. Shokin, and M. Sladkevich (2009), The 1956 Greek tsunami recorded at Yafo, Israel, and its numerical modeling, *J. Geophys. Res.*, *114*, C09002, doi:10.1029/2008JC005262.

1. Introduction

[2] About 300 descriptions of tsunamis and similar phenomena are known for the Mediterranean Sea [Soloviev *et al.*, 2000]. Historical records show that the Eastern Mediterranean is more prone to damaging tsunamis than the western one. The strongest tsunamis are excited in the Aegean Sea, the Hellenic and Calabrian arcs. Greece and the surrounding regions have long been affected, with more than 160 events having been cataloged over the past 2000 years [Ambraseys and Jackson, 1990; Ambraseys, 2008]. The main tsunamigenic sources were located in the

Sicily region, Aegean Sea and Cyprus. Moreover, there is historical evidence that some of tsunami sources were located near the coastal region of Israel.

[3] The available information related to tsunamis in Israel [Amiran *et al.*, 1994; Guidoboni and Comastri, 1997; Reinhardt *et al.*, 2006; Salamon *et al.*, 2007] is mostly descriptive with no attempts to conduct comprehensive numerical simulations of tsunami waves until recently. Only relatively strong oscillations, which can be identified as tsunami waves caused by significant earthquake in the Aegean Sea dated 9 July 1956 have been recorded in Israel by a floating-type tide gauge installed in Yafo Port [Goldsmith and Gilboa, 1986]. Similar records of the water surface displacements measured by tide gauges have been reported by Ambraseys [1960] at Laki station (Leros Island) and Souda station (Crete Island). While the Yafo record can be classified as far-field (at distance of above 700 km from the epicenter) event, the last two, are near-field events. The current paper deals with analysis of the Yafo record of the 1956 tsunami waves and their numerical modeling. Also, the recent digitally recorded tide-gauge measurements of sea level oscillations in the vicinity of the Israeli coast are processed and analyzed to determine the periods of resonant seiches on the continental shelf, which can amplify tsunami wave amplitudes in the coastal locations. The paper is

¹Institute of Computational Technologies, Siberian Branch of the Russian Academy of Sciences, Novosibirsk, Russia.

²Department of Mechanics and Applied Mathematics, Institute of Cybernetics, Tallinn University of Technology, Tallinn, Estonia.

³School of Mechanical Engineering, Faculty of Engineering, Tel Aviv University, Tel Aviv, Israel.

⁴Also at Coastal and Marine Engineering Research Institute, Technion City, Haifa, Israel.

⁵Coastal and Marine Engineering Research Institute, Technion City, Haifa, Israel.

⁶Department of Nonlinear Geophysical Processes, Institute of Applied Physics, Russian Academy of Sciences, Nizhny Novgorod, Russia.

organized as follows: Section 2 describes the Greek tsunami of 9 July 1956 and presents an analysis of its unique far-field record made in Yafo. Section 3 deals with spectral analysis of the sea level oscillations at three points (Ashdod, Tel Aviv, Acre) located along the Israeli Mediterranean coast. Section 4 gives a brief description of the mathematical models applied for simulation of tsunami generation, longwave propagation and shelf resonance modeling; while the details of the numerical scheme are presented in Appendix A. Section 5 provides the results of the numerical modeling of the 1956 tsunami. Section 6 contains concluding remarks.

2. Greek Tsunami of 9 July 1956

2.1. Historical Data and Estimation of Tsunami Travel Times

[4] The historical information about tsunamis in Israel is limited and mostly based on eye witness reports [e.g., *Amiran et al.*, 1994; *Salamon et al.*, 2007]. Moreover, there is almost no detailed information that can make quantitative numerical simulation of these events possible. The Permanent Service for Mean Sea Level (UK) made a unique measurement of far-field water level fluctuations in Israel from the 1956 tsunami event.

[5] During this event the waves engulfed mainly the Greece coast, Amorgos Island, and other Aegean Islands. Away from the epicentral area, the waves attenuated rapidly, to 2.5-m runup on the eastern coast of Crete and small amplitudes recorded on the Egyptian and Israeli Coasts. According to *Ambraseys* [1960], at the southeast coast of the Amorgos Island waves up to 100 feet (30 m) in height crashed against the rocky cliffs. At different locations near the epicentral region the waves caused boats being driven onto docks, houses flooded and three persons reported drowned. *Okal et al.* [2004] reported on a systematic survey of tsunami runup heights in the Aegean Islands and the Asia Minor Coast of Turkey, through the interview of elderly witnesses of the tsunami following the protocol discussed by *Synolakis and Okal* [2005]. Their growing data set presently includes 29 data points on seven islands and at eight villages on the Turkish Coast. They confirmed a single runup value of 20 m on Eastern Amorgos, with measured runup limited to 8 m on Astypalaia and at most 3 m at other locations (1 m on the Turkish Coast). Similar results were reported in a recent paper by *Camilleri* [2006]. In a more recent paper, *Okal et al.* [2009] report a total of 68 points including runup of 14.6 m in Folegandros.

[6] The 1956 tsunami triggered by an earthquake in the Aegean Sea was the largest and most destructive to have occurred in Greece during the twentieth century [*Stiros et al.*, 1994]. The magnitude ranges from 7.2 to 7.8 depending on information source. According to *Ambraseys* [1960, p. 1261] “the earthquake which preceded or coincided with the seismic sea wave of 9 July 1956 occurred at 03 11 38 GMT (Local time = GMT + 2 hours) with an epicenter at 36°54′N, 26°00′E. The magnitude of the shock was $7\frac{1}{2}$, and it was followed, at 03 24 05 GMT by a strong aftershock of magnitude 7, the epicenter of which was at 36°48′N, 25°12′E.” The above data are used in our subsequent numerical computations. *Perissoratis and Papadopoulos* [1999] claim that the epicentral location of the main shock

was about 20 km to the south of the Amorgos Island, while the main aftershock was located about 5 km ENE of the Santorini Island. According to the map provided by these authors the epicenter of the main shock with $M = 7.5$ was at 36°39′N, 25°54′E and of the main aftershock with $M = 7.2$ at 36°27′N, 25°31′E, which is inconsistent with the coordinates given in the work of *Ambraseys* [1960]. Somewhat different coordinates (36°42′N, 25°48′E) of the main shock with magnitude 7.5 appeared in the Integrated Tsunami Database for the World Ocean (WinITDB; see http://tsun.sccc.ru/tsun_hp.htm). The above mentioned locations of the earthquake epicenter are shown in Figure 1. Other sources and their locations are discussed in detail in the work of *Okal et al.* [2009].

[7] The tsunami-wave travel time from the source to various locations in the Eastern Mediterranean was calculated using a model incorporated in WinITDB with bathymetry from GEBCO (1-min resolution; available at <http://www.gebco.net/>). In Figure 1 the isochrones from the 1956 tsunami source are drawn every 10 min. Our estimates show that in the far field the wave travel time to the Cyprus Island is about 1.30 h, to Haifa 2.10 h, and to Tel Aviv-Yafo 2.20 h.

[8] Isochrones within the Aegean Sea were computed using the WinITDB system and more detailed bathymetry obtained by interpolation of the GEBCO bathymetry. The initial perturbation is modeled here by an ellipse with its principal axis coinciding with the trough of the submarine trench of Amorgos as suggested by *Ambraseys* [1960]. Figure 2 compares the computed isochrones with those presented by *Ambraseys* [1960]. The tsunami-wave travel time from the source to Leros and to the northern coast of Crete calculated using the WinITDB system is ~20 and 50 min, respectively, which is in good agreement with the arrival time estimated from *Ambraseys*'s map.

2.2. Short Description of Yafo Port, Tidal Gauge, and Data Handling of the Tsunami Record

[9] In 1956, the sea level was recorded by the Permanent Service for Mean Sea Level using a float-type tide gauge installed within the Yafo fishing port (Cape Yafo station). Yafo (32°18′N, 34°27′E) is a city located south of Tel Aviv and today is a part of the Tel Aviv-Yafo municipality. The layout of Yafo harbor is shown in Figure 3, and the sounding are in meters. The water depth in the harbor is about 3 m, and this depth was also maintained at the port entrance (Figure 3b). The main breakwater length of the gaunt alongshore Yafo harbor is about 400 m, and maximum width of the harbor does not exceed 150 m.

[10] The tide-gauge records during 8–9 July 1956 at the Yafo gauge station are shown in Figure 4. *Goldsmith and Gilboa* [1986] suggest that the water level oscillations due to this tsunami started on 9 July 1956 at 0900 Israeli local time (GMT + 3 hours, since the clock in Israel was adjusted to daylight saving time (DST) during years 1948–1957 and then the use of DST was renewed in 1990s) and lasted 2 days. The characteristic period was 12–15 min and maximum height of oscillations was 28 cm.

[11] The records of sea level fluctuations recorded on 9 July 1956 at the Yafo port are shown in Figure 5 along those presented by *Ambraseys* [1960], i.e., the measurements at Laki (Leros) and Souda (Crete). According to *Ambraseys* [1960], both the Laki and Souda gauges were

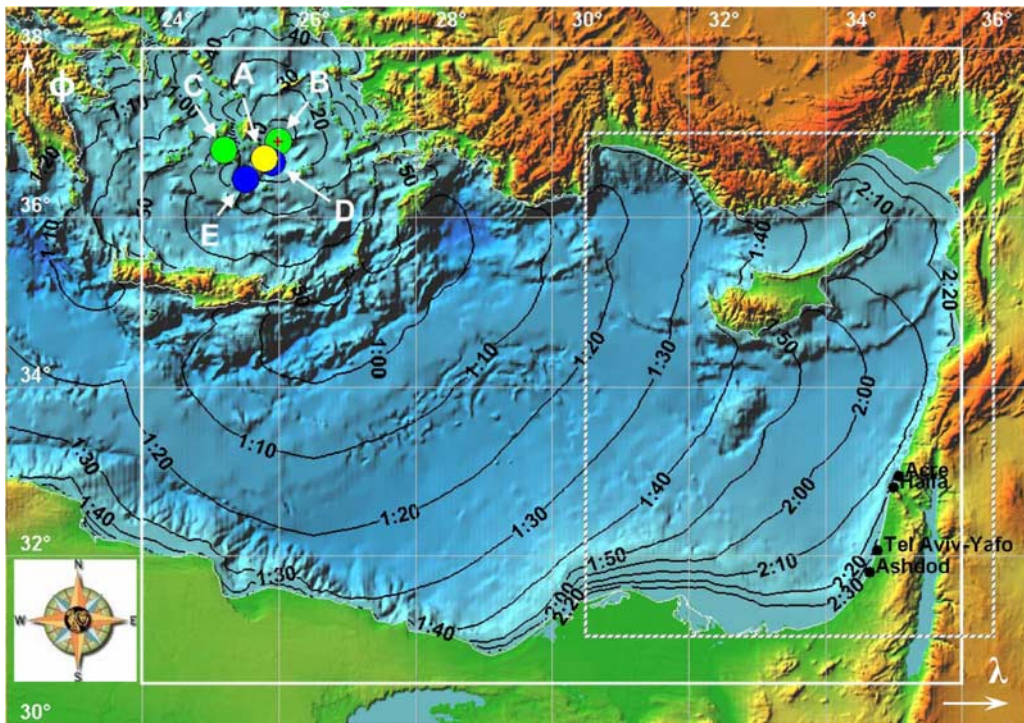


Figure 1. Map of locations of the 1956 earthquake epicenter. The letter A depicts the main shock at $36^{\circ}42'N$, $25^{\circ}48'E$, according to WinITDB (see http://tsun.sccc.ru/tsun_hp.htm). The letters B and C depict the main shock at $36^{\circ}54'N$, $26^{\circ}00'E$, and the aftershock at $36^{\circ}48'N$, $25^{\circ}12'E$, according to *Ambraseys* [1960], respectively. The letters D and E depicts the main shock at $36^{\circ}39'N$, $25^{\circ}54'E$, and the aftershock at $36^{\circ}27'N$, $25^{\circ}31'E$, according to *Perissoratis and Papadopoulos* [1999], respectively. The tsunami isochrones are computed assuming the earthquake epicenter location at B. The area for tsunami propagation study is marked by the solid rectangle, whereas the dashed rectangle represents the area for shelf resonance study.

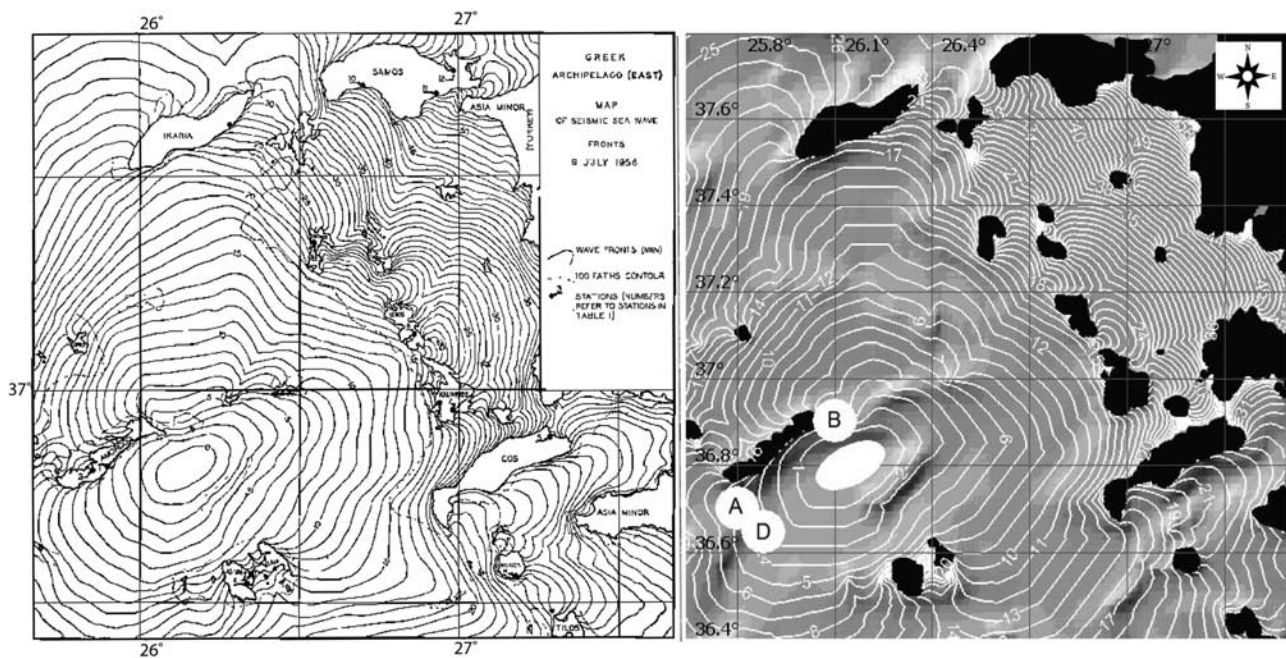


Figure 2. Comparison between isochrones within the Aegean Sea extracted from *Ambraseys* [1960] and computed using the WinITDB system. Only locations of the main shocks are shown. A, $36^{\circ}42'N$, $25^{\circ}48'E$, according to WinITDB (see http://tsun.sccc.ru/tsun_hp.htm); B, $36^{\circ}54'N$, $26^{\circ}00'E$, according to *Ambraseys* [1960]; D, $36^{\circ}39'N$, $25^{\circ}54'E$, according to *Perissoratis and Papadopoulos* [1999].

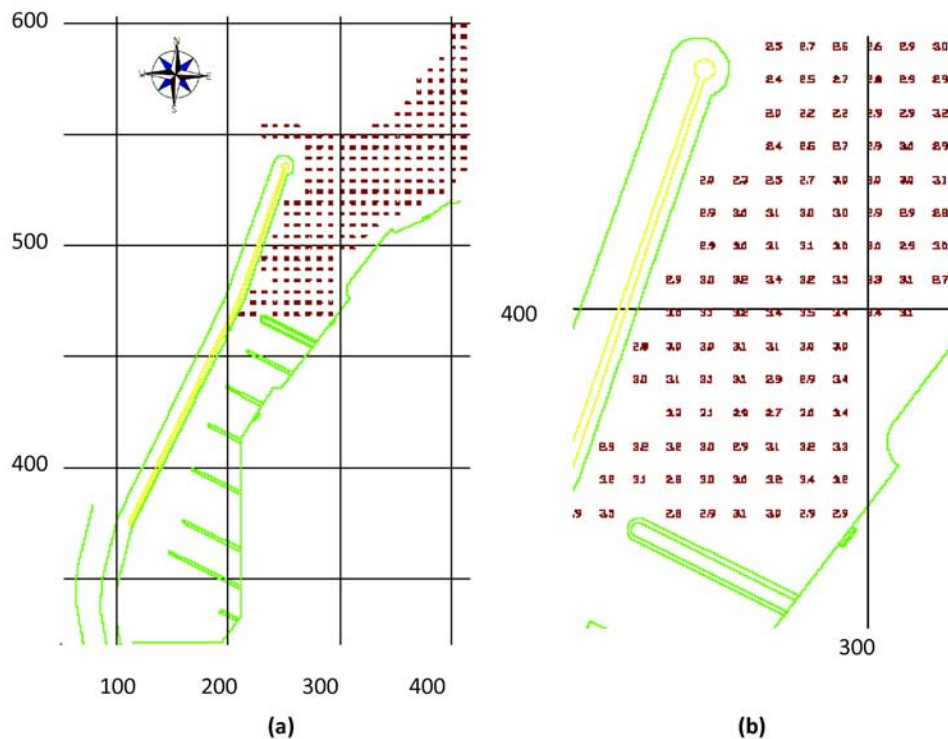


Figure 3. Sketch of the Yafo port: (a) general plan view and (b) zoom of the port entrance. The scale and the sounding are in meters.

rendered temporarily useless by the seismic shock, thus, the initial part of the marigram is missing. The Yafo marigrams indicate that the intensive (abnormal) high-frequency sea level oscillations started at ~ 0535 GMT, i.e., 2 h, 23 min after the main shock and 2 h, 11 min after the aftershock, which is consistent with the WinITDB assessment of 2 h, 20 min. Moreover, as it is clearly seen from Figure 5, the number of peaks during the same period of time (6 h) is the same for all stations (Laki, Souda and Yafo) and, consequently, the period of these fluctuations, is almost the same. This increases significantly our confidence in the common origin of all three waves' records and thus supports our assumption that the oscillations recorded at Yafo are associated with the tsunami event of 9 July triggered by the earthquake in the Aegean Sea, and not by barometric forcing.

[12] A day before the tsunami, on 8 July 1956, the high-frequency sea level oscillations on the record represent probably stationary random noise with almost constant amplitude (4-cm height). Plot of the records dated 9 July are digitized with the time step of 30 s (plot with the records of 8 July are not used owing to their poor temporal resolution). Tide elimination is performed using the Godin-type filter [Emery and Thomson, 1997] and described in the work of Pelinovsky *et al.* [2005]. The tidal component of the records is computed using three consecutive running-mean filters with windows 35, 35 and 40 min. Then, the selected tide component is subtracted from the initial record. Digitized records with and without tide are presented in Figure 6.

[13] The energy spectrum of the high-frequency oscillations of the 9 July records (Figure 7) is obtained using standard fast Fourier transform (FFT) procedure. Digitized records with and without tide are used in the spectral

analysis. As expected, both records provide identical results in the high-frequency range composed of tsunami waves and shelf-resonance oscillations. The spectrum of the raw record (not shown here) contains high peak component at low frequency corresponding to dominant semidiurnal oscillations, however, the separation between these two ranges is large enough to make mutual interference impossible. The higher-frequency range of the spectrum contains the dominant peak related to the period of ~ 15 min, which can be associated with the tsunami event. The other minor components include a constituent that corresponds to the period of about 57 min, the origin of which, as will be shown in sequel, can be related to shelf resonance. It should be noted that the groin on the left of Yafo harbor with length ~ 400 m and water depths ~ 3 m implies harbor resonance periods of about 5–6 min. Therefore, neither dominant period in the record can be associated with harbor resonance.

3. Spectral Analysis of Sea Level Records

[14] As explained above, the record obtained a day before the tsunami, has very low temporal resolution and hence cannot be used for analysis of the tide high-frequency oscillations always present at the continental shelf. These shelf oscillations may be attributed to meteorological forcing. In order to reveal harmonics related to continental shelf resonance, spectral analysis of sea level fluctuations measured recently by the Israeli National Agency for Geodesy, Cadastre, Mapping and Geographic Information Systems, is performed. The instruments used in continuous digital recording of seawater level are modern high-resolution tidal gauges. The data include measurements at Tel Aviv during 1996 and 1997, at Ashdod during 2000 and 2005, at Acre

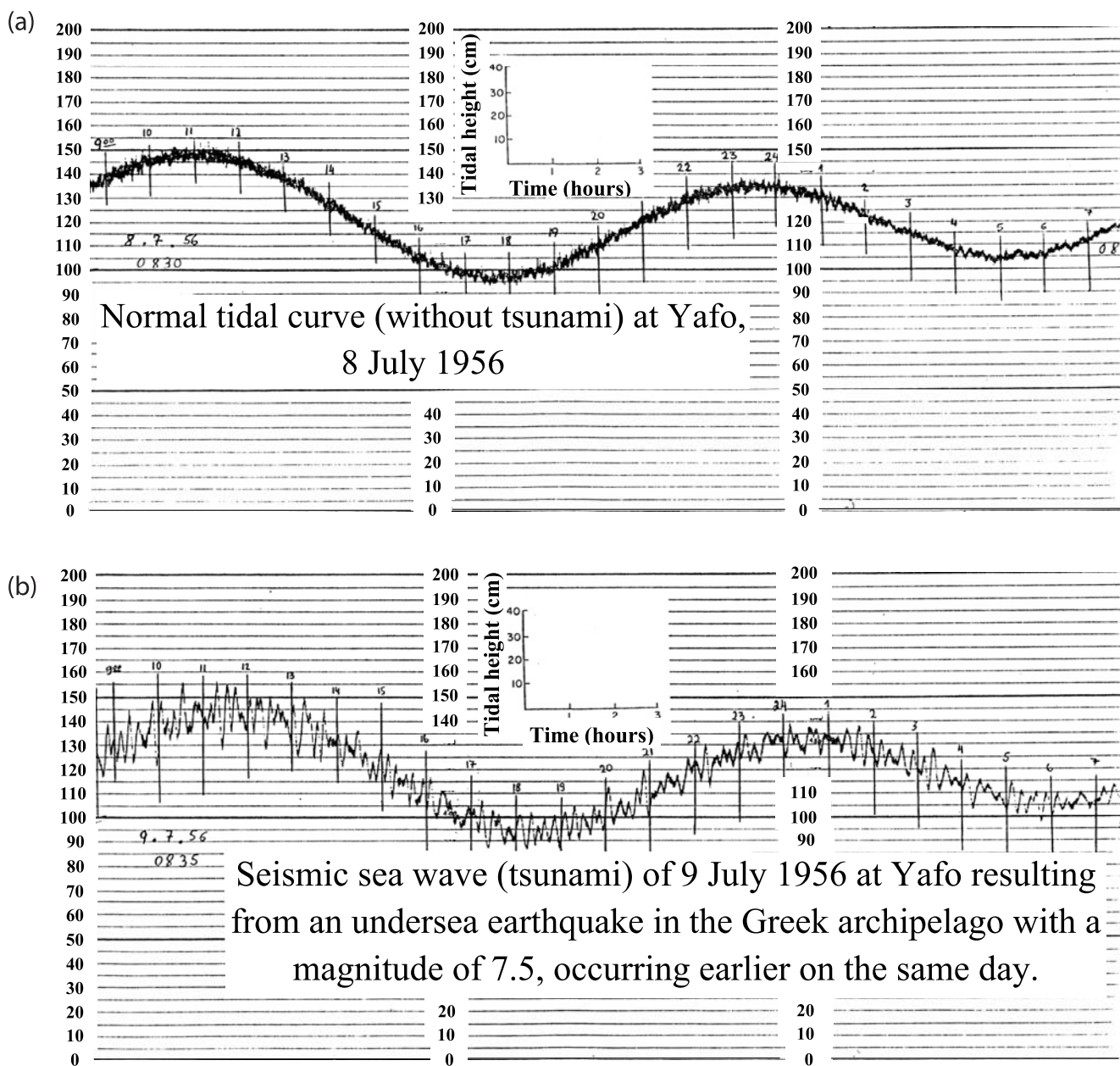


Figure 4. (a) Tide-gauge records at Yafo a day before tsunami on 8 July 1956 and (b) tsunami records on 9 July 1956. The horizontal axis represents local time in hours and the vertical axis represents sea level in centimeters. The time appearing on the plots is the local Israeli time. To obtain GMT time, 3 hours should be subtracted (the clock in Israel was adjusted to daylight savings time (DST) during years 1948–1957).

during 2005, and were provided to us by the Israeli National Agency.

[15] The Levant coast is dominated by semidiurnal tides with longer-period (diurnal, fortnight, monthly, and semi-annual) components and higher-frequency harmonics that correspond to shelf resonance. The great advantage of the data acquired by the Israeli National Agency is continuous digital recording of the water level oscillations, which enables one to perform averaging of spectra over long period of time to obtain very reliable estimates of the high-frequency constituents. The sampling at the Tel Aviv tide gauge was 10 min, and at Ashdod and Acre it was 5 min.

According to the Nyquist–Shannon sampling theorem, the lowest measurable period (highest frequency) is 20 min for Tel Aviv and 10 min for Ashdod and Acre records. The processing of the data was performed via FFT and IFFT (direct and inverse fast Fourier transformation, respectively) using MATLAB. The spectral analysis of the high-frequency oscillations with tide eliminated from the initial signal shows that the spectra at all locations contain 50- to 60-min periods (see Figure 8), which are likely due to continental shelf resonance. These seiche associated periods are further verified through the numerical simulations, which are presented in the sequel.

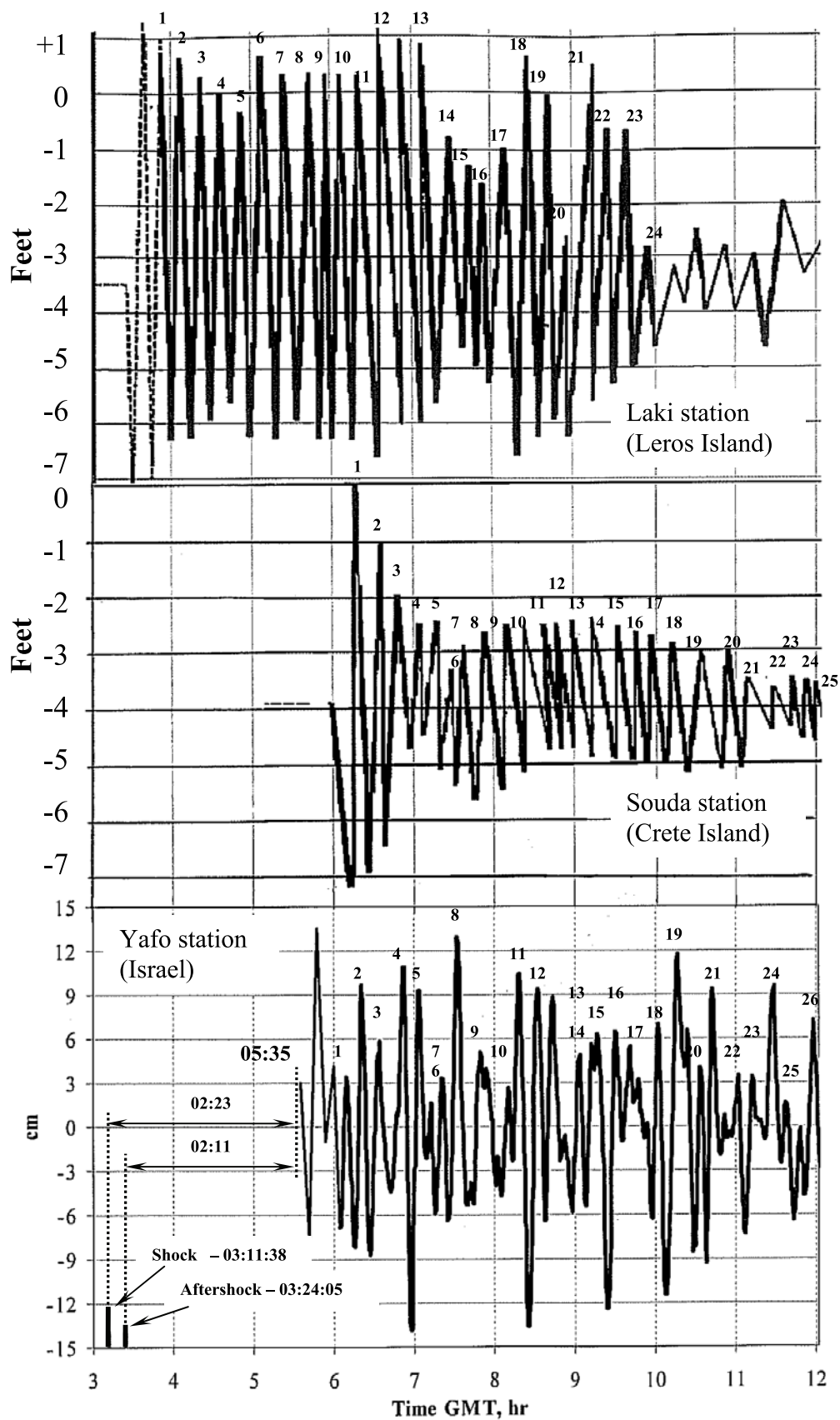


Figure 5. Comparison between three marigrams recorded by tide gauges at Laki, Souda, and Yafo stations on 9 July 1956. The upper two marigrams (Laki and Souda) are extracted from *Ambraseys* [1960].

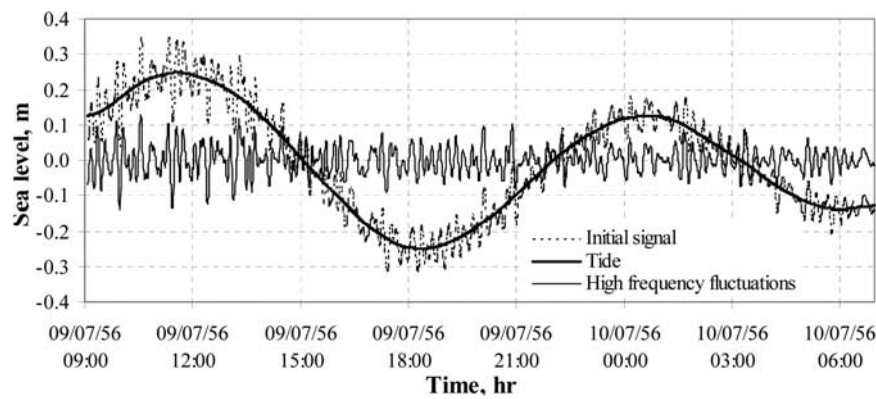


Figure 6. Digitized tide-gauge record of 9 July 1956. The initial record with eliminated constant level of 1.19 m is depicted by the dashed line; the tidal component is depicted by the bold solid line; and the high-frequency fluctuations due to tsunami are depicted by the solid line. Time is given by Israeli local time (GMT + 3 hours).

[16] *Pattiaratchi and Wijeratne* [2009] reported tide-gauge records with periods ranging from minutes to hours in Colombo, Sri Lanka, and Geraldton, Australia. For the disastrous 2004 tsunami in the Indian Ocean, the higher-frequency waves had energy in the periods ranging from 20 to 85 min with dominant constituents between 35 and 60 min. As a result of the tsunami impact, the energy contained in these periods was increased by 2–3 orders of magnitude. In particular, spectral analysis of the data obtained in Colombo before and immediately after each of the tsunamis in 2004, 2005 and 2007 indicate that the energy component with period of 75 min was enhanced by few orders during the tsunamis. The authors claim that although the tide gauge was located inside the harbor, the 75-min oscillations are related to the local effects on the entire continental shelf.

[17] The fundamental mode determining shelf oscillations can be estimated using a simple model that describes the shelf resonance as a standing wave with a node at the edge of the shelf and an antinode at the coastline. The period of the dominant mode is $T = 8\sqrt{l/(s \cdot g)} = 8l/\sqrt{gh}$, 4 times the travel time from the shore to the shelf edge [*Munk*, 1962]. Here l is the shelf width, s is the continental shelf slope, g is the acceleration of gravity, and h is the water depth at the shelf edge. It is obvious that in the case of a horizontal shelf

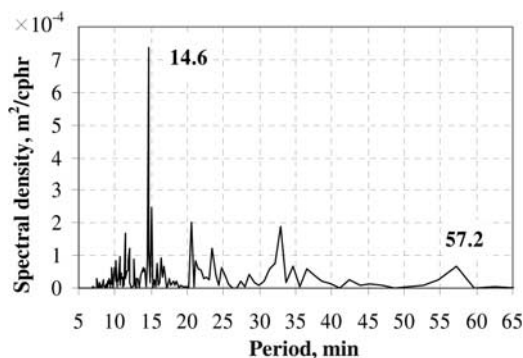


Figure 7. Energy spectrum of the high-frequency fluctuations (tide is eliminated) of the sea level records at the Yafo floating-type tide gauge on 9 July 1956.

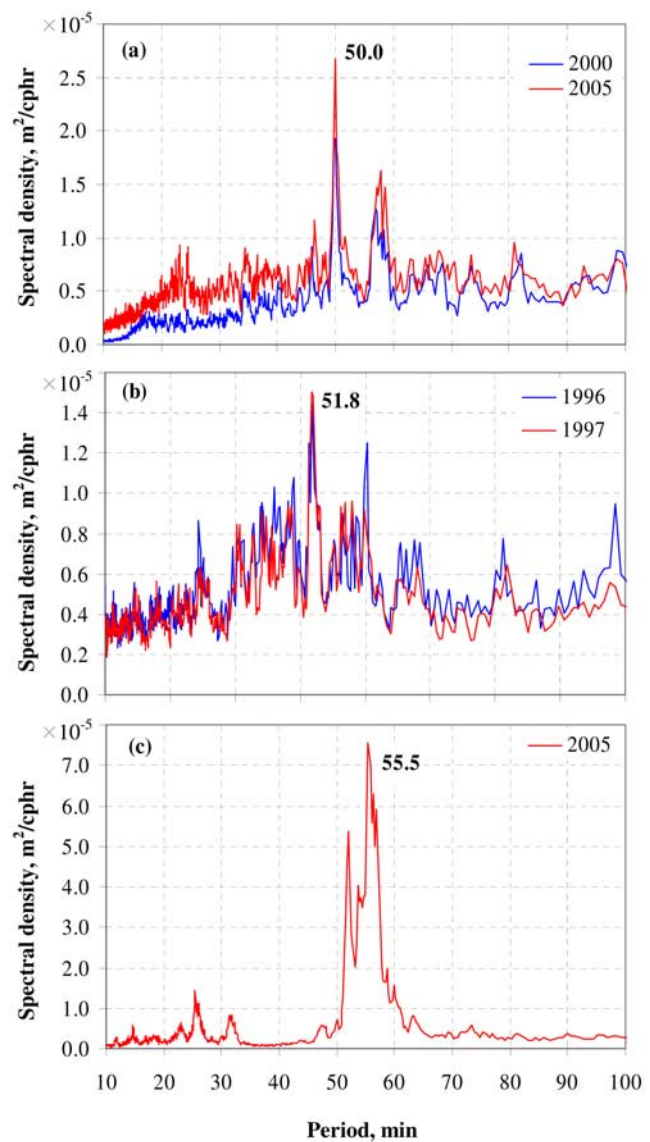


Figure 8. Spectrum of the high-frequency oscillations (tide is eliminated) of the sea level records (a) during 2000 and 2005 at the Ashdod gauge; (b) during 1996 and 1997 at the Tel Aviv gauge; and (c) during 2005 at the Acre gauge.

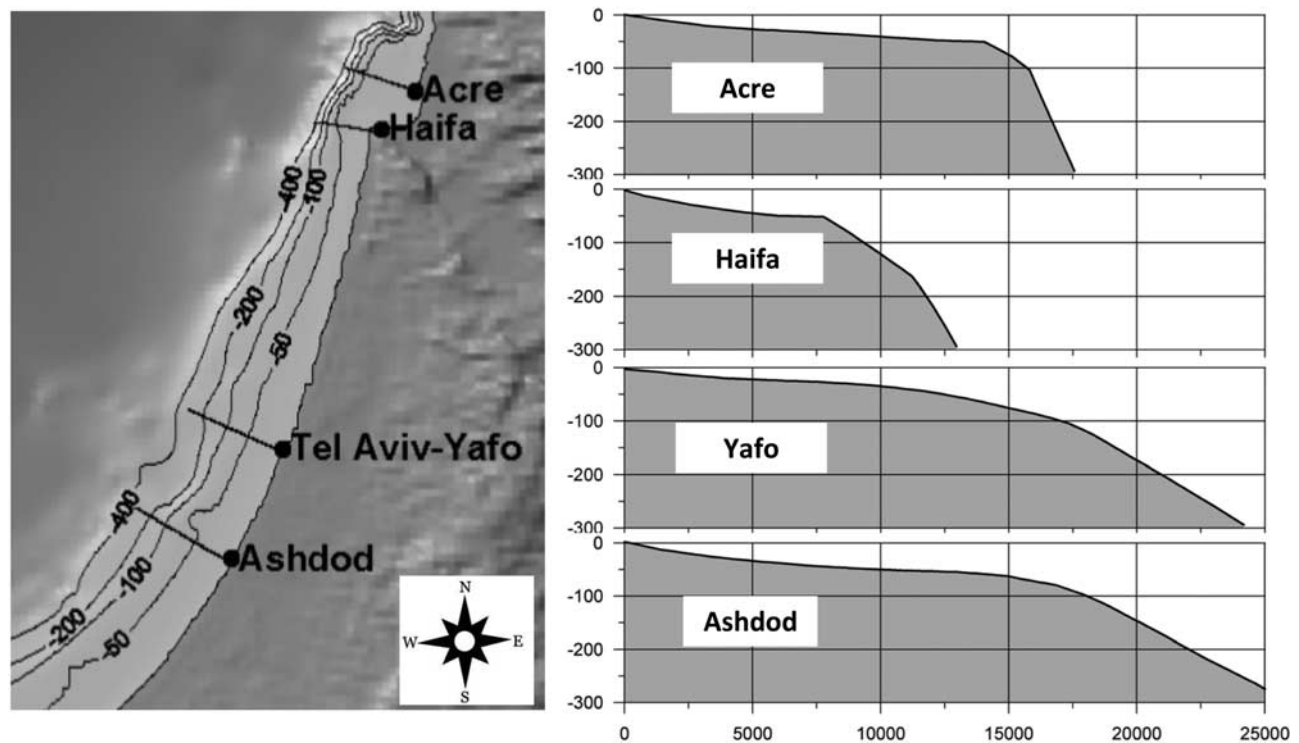


Figure 9. (left) Map showing shelf bathymetry and location of the extraction points used in this study and (right) the cross-shore profiles offshore Ashdod, Yafo, Haifa and Acre marked by the lines in the left panel. The scale is in meters.

with almost a vertically beach, the resonant period becomes $T = 4l/\sqrt{gh}$ near to the coastline. The slope of the Israeli shelf is moderate in the southern part of the coast and steeper to the north up to the Haifa Bay. According to our estimations based on the analysis of cross-shore profiles (see Figure 9), the edge of the Israeli continental shelf with 100 m depth, varies moderately (Table 1) providing continental shelf slopes of 0.005–0.007. However, typical near-shore slopes estimated using local bathymetric maps are steeper and vary from 0.010 to 0.015, indicating significant slope variations across the shelf. Therefore only very rough estimate of the shelf period can be obtained using either of the above formulas. Nevertheless, it is interesting to compare these estimates to the periods of the analyzed spectra to shed light on the spectral peaks. As can be seen from Table 1, the agreement is reasonable. Other researchers [e.g., *Van Dorn*, 1987; *Yanuma and Tsui*, 1998; *Galton-Fenzi et al.*, 2006] have reported similar effects attributed to a coastal seiche.

[18] Clearly, the 15-min periods in the 1956 Yafo record (see Figure 7) do not appear in the spectra of recent sea level measurements. This issue is discussed later.

4. Mathematical Model

[19] The mathematical model applied for the numerical simulations can be split into two main blocks: (1) the model of tsunami generation by a tsunamigenic earthquake, and (2) the model of tsunami wave propagation.

[20] Two modeling steps are necessary for accurate description of tsunami generation: a model for the earthquake fed by the various seismic parameters, and a model for the

formation of surface gravity waves resulting from the deformation of the seafloor [e.g., *Synolakis and Bernard*, 2006; *Kervella et al.*, 2007, and references therein]. For the resulting water motion, the standard practice is to transfer the inferred seafloor displacement to the free surface of the ocean. This approach called by *Kervella et al.* [2007] as the passive generation approach leads to a well-posed initial value problem with zero velocity. An open question for tsunami forecasting modelers is the validity of neglecting the initial velocity. In a recent note, *Dutykh et al.* [2006] used linear theory to show that, in fact, differences may exist between the standard passive generation and active generation, which take into account the dynamics of seafloor displacement.

[21] The numerical experiments have been conducted on the grid with 1 arc min bathymetry resolution as well as on

Table 1. Estimates of Shelf Resonance Periods

Parameter	Ashdod	Tel Aviv-Yafo	Haifa	Acre
Water depth (m)	100	100	100	100
Distance from the coastline (km)	17.0	14.0	9.5	15.5
Periods calculated using Munk's formula (min)	72	60	40	66
Periods calculated from the sea level records (min)	50.0	51.8	no data	55.5
Periods calculated from the numerical simulations (min)	54–63	53.6	55.6	57.7

the refined 30"-, 20"-, 15"-, and 7.5"-grids obtained via interpolation of the 1-min grid. In the following computations only the 1-min and 15-s grids are involved. The bathymetry is obtained using the Naval Oceanographic Office Bathymetry available at <http://ferret.pmel.noaa.gov/NVODS/servlets/constrain?var=17718>. In the vicinity of the Israeli coast, the bathymetry was replaced by more accurate data obtained from the local sources, in particular, measured by OCEANA Ltd. and available at <http://israel-business.dundb.co.il/CompanyPageNo.aspx?Duns=600068530>.

4.1. Tsunami Generation

[22] The selection of appropriate tsunami sources is always difficult and requires good knowledge of the regional geology and understanding of earthquake mechanisms. In this respect there is not a complete agreement between researchers about the mechanism of the 1956 tsunami generation (see *Okal et al.* [2009] for a comprehensive discussion).

[23] According to *Ambraseys* [1960], the steep slopes of deposits on the banks of the submarine trench of Amorgos could easily slide under the influence of a shock as intense as that of 9 July. *Ambraseys and Jackson* [1990] suggest that the sea wave was probably generated by either a submarine slide in the Amorgos basin, which has a depth of about 500 m, or by faulting of the seabed. *Perissoratis and Papadopoulos* [1999] arrived at a similar conclusion that an adequate reproduction of the near-field maximum wave amplitudes observed during the 1956 tsunami requires not only a coseismic seafloor fault displacement but also an additional tsunamigenic component. *Okal et al.* [2004] report on a new survey of tsunami runup heights in the region of the earthquake. On the basis of confirmed single runup values of 20 m on Eastern Amorgos they conclude that the uniqueness of the large runup value, in the proximity of locales with milder values, does suggest that it was due to the influence of a localized underwater landslide. *Okal et al.* [2009] further underscore the hypothesis and present several candidate landslides to explain the observed extreme runup in Folegandros and Astypalaia.

[24] In the following we make an attempt to compare the tsunamigenic source and the consequences of the Greek 1956 tsunami with the Papua New Guinea (PNG) 17 July 1998 tsunami. According to *Tappin et al.* [2008, p. 262], "PNG remains the only tsunami clearly identified as caused by a submarine slump. It is a benchmark case." The tragic event began with an estimated 7.0 magnitude earthquake at 0849 GMT in the Sandaun province of northwestern Papua New Guinea. Several aftershocks and the tsunami occurred about 20 min later. A considerable amount of research has been devoted to careful surveys of marine geology, data analysis, and tsunami source modeling using both coseismic and a submarine slumps.

[25] *Kawata et al.* [1999] report the findings of the International Tsunami Survey Team which started a week-long investigation 31 July 1998. The team was able to precisely map the inundation and establish that extremely flows were limited to fairly narrow section of the shoreline. Maximum wave heights of 15 m and overland velocities of 15–20 m/s along a 25-km stretch of coastline were confirmed. According to them, the probable geometry of rupture, as inferred from the location of the main shock

and aftershock, was difficult to reconcile with the concentration to the east of the seismogenic zone, unless exceptional focusing by unexpected bathymetric features was involved. By assuming a landslide source, they found that a tsunami could be generated by the motion of $\sim 10 \text{ km}^3$ of sediments and thus could explain the localization of the devastation.

[26] Alternative source mechanisms of the tsunami were addressed in the work of *Tappin et al.* [2001] and *Matsumoto et al.* [2003]. Their investigations were based on an offshore survey using multibeam bathymetry, subbottom profiling, sediment sampling, and observation by means of remote operated vehicles (ROV) and submersibles. Their offshore data allowed identification of a sediment slump located offshore. The authors observed recent seabed movement in the form of fissures, brecciated angular sediment blocks, and vertical slopes within an accurate amphitheater-shaped structure, which give evidence in favor of slump presence at this location. The conducted numerical modeling supports the suggested slump movement over the fault displacements as the tsunami generation source.

[27] *Gelfenbaum and Jaffe* [2003] reported on detailed measurements of coastal topography, tsunami flow height and direction indicators, deposit thickness made in the field, and on samples of the deposit collection for grain-size analysis in the laboratory.

[28] *Synolakis et al.* [2002] based their analyses of tsunami amplitude and timing on available bathymetric and seismic images that support the scenario of the generation of the PNG tsunami by a large underwater slump at 0902 GMT and attribute the delay of 13 min between the main shock and the initiation of the slump to the nucleation of failure in the sedimentary mass.

[29] *Okal* [2003a] investigated the seismic events which took place between the main shock at 0849 GMT and the main aftershock doublet at 0909–0910, and presented evidence that an event detected at 0902 GMT involved a major slump, which he proposed as the source of the tsunami. This evidence was based on the analysis and seismic *T* waves recorded at various sites around the Pacific from the 0902 event.

[30] *Okal* [2003b] explored theoretically the differences in far-field tsunami excitation by dislocation and landslide sources. He showed that the spectrum of landslide-generated tsunamis is expected to be shifted to relatively high frequencies (10 mHz), where dispersion effects act to further reduce significantly far-field amplitudes. This frequency is very high compared to our estimates that reveal a frequency of about 1.0 mHz at all tide gauges (Laki, Souda, and Yafu; see Figure 5).

[31] *Okal and Synolakis* [2004] compared the 1998 PNG tsunami with the 2002 tsunami of Wewak, also occurred in Papua New Guinea. They found that though the 2002 earthquake was more destructive (in terms of structural damage) than the 1998 earthquake, the 2002 tsunami did not produce nearly as large a runup as the 1998 tsunami did, most likely because the 2002 earthquake did not produce a significant landslide. This is further supported by the fact that moderate runup for the 2002 tsunami was found over a larger geographical area than for the 1998 tsunami, showing that the earthquake generated tsunami was less affected by radial damping. These two earthquakes featured strikingly

Table 2. Dislocation Parameters

Parameter	Computed Using Equations (1)			Computed Using Equations (2)
	Scatter by Sigma (Lower Bound)	Mean Value of Coefficient	Scatter by Sigma (Upper Bound)	
a_L	-1.36	-2.01	-2.66	-1.9
b_L	0.40	0.50	0.6	0.5
a_W	-0.86	-1.14	-1.42	-2.2
b_W	0.30	0.35	0.40	0.5
a_{h_0}	-2.86	-4.45	-6.04	-3.2
b_{h_0}	0.39	0.63	0.87	0.5
M	7.5	7.5	7.5	7.5
L , km	43.65	54.95	69.18	70.79
W , km	24.55	30.55	38.02	35.48
h_0 , m	1.16	1.88	3.05	3.55
M	7.8	7.8	7.8	7.8
L , km	57.54	77.62	104.71	100
W , km	30.20	38.90	50.12	50.12
h_0 , m	1.52	2.91	5.57	5.01

differing damage, even though their epicenters were only 120 km apart, i.e., the 1998 event did practically no structural damage, but its tsunami was devastating, while the stronger 2002 event resulted in widespread destruction, but generated only a benign tsunami. By carrying out simulation of the runup of a near-field tsunami along a beach for more than 70 scenarios of both dislocation and landslide sources they showed that the aspect ratio I_2 representing the ratio of the maximum runup η to the characteristic width a_w of its distribution along the beach is a robust discriminant between the two families of sources. Even in a worst case scenario, they found that I_2 remains less than 10^{-4} while landslide sources lead to higher values of I_2 for all physically realistic combinations of source parameters. They also suggest using scalar I_1 , which scales the ratio of the maximum runup to the seismic slip h_0 , as a further discriminant of the nature of the source. It is easy to obtain real-time estimates of the seismic slip h_0 , and thus a value of I_1 can be inferred from a field survey. Their analyses show that excessive values of I_1 , corresponding to runup amplitudes reaching 5 times or more the values of the slip h_0 are simply incompatible with tsunami generation by a dislocation.

[32] *Lynett et al.* [2003] compared the Boussinesq model and a nonlinear shallow water wave (NLSW) model in order to quantify the effect of frequency dispersion on the landslide-generated tsunami. The numerical comparisons indicate that the NLSW model is a poor estimator of offshore wave heights. It is most probably related to high frequency in this specific case. Therefore we do not expect effect of dispersion in our simulations of the 1956 Greek tsunami.

[33] *Harbitz et al.* [2006] show that frequency dispersion is of little importance for waves generated by large and subcritical submarine landslides. According to these authors tsunamis generated by submarine landslides often have very large runup heights close to the source area, but have more limited far-field effects than earthquake tsunamis. They further show that the combination of landslides and earthquakes may be necessary to explain the observed tsunami behavior. The aspects mentioned above are exemplified in their study by simulations of the Holocene Storegga Slide,

the 1998 Papua New Guinea, and the 2004 Indian Ocean tsunamis.

[34] Three important conjectures may be made on the basis of the above review: (1) There is a strong necessity to use the discriminants I_2 and I_1 to determine the source of tsunami [*Okal and Synolakis*, 2004]; (2) there is a vital need for as much as possible field surveys to collect relevant geological data and evidences from witnesses [*Synolakis and Okal*, 2005]; and (3) the possible discrepancy between observed and simulated tsunami wave amplitudes could be explained by considering that the tsunami source includes two components of tsunami genesis: a coseismic fault displacement and a seismically triggered massive sediment landslide. Evaluation of I_1 for 1956 Greek tsunami yields a value of about 6 and seems to be incompatible with tsunami generation by a dislocation. In this sense, a combined action of a coseismic tectonic displacement associated with the 1956 main shock and its largest aftershock, which took place 13 min after the main shock, and of a massive sediment landslide triggered by the first and/or the second of those seismic events, should be considered as a more probable tsunamigenic source of the 1956 event. This paper considers both possible tsunami generation mechanisms: (1) coseismic and (2) sediment landslide.

[35] The main model parameters, the fault length L , the fault width W , and the bottom displacement h_0 , are calculated using the relationships (1) given in the work of *Wells and Coppersmith* [1994] and (2) provided by *Japan Meteorological Agency (JMA)* [2001]:

$$\begin{aligned} \log(L) &= a_L + b_L M, & \log(W) &= a_W + b_W M, \\ \log(h_0) &= a_{h_0} + b_{h_0} M \end{aligned} \quad (1)$$

$$\begin{aligned} \log(L) &= -1.9 + 0.5M, & \log(W) &= -2.2 + 0.5M, \\ \log(h_0) &= -3.2 + 0.5M. \end{aligned} \quad (2)$$

[36] The coefficients in expressions (1) are selected using the table given in the work of *Wells and Coppersmith* [1994] and the fault length; its width and the bottom displacement have been calculated and compared with those obtained using equations (2). It can be seen from Table 2 that the latter values are in the range of scatter of the values computed using equations (1) as given in the work of *JMA* [2001].

[37] In the framework of this study the computational procedure of residual displacements adopts the model derived by *Gusiakov* [1978], which provides the results similar to those that would be obtained by using the model proposed later by *Okada* [1985], i.e., the results are within the accuracy of numerical algorithms performance on different computers.

[38] The detailed landslide movement is not modeled in the course of this study. To assess tsunami wave parameters caused by the landslide, its characteristics have been selected on the basis of the initial ellipse above Amorgos submarine trench, which was adopted from *Ambraseys* [1960] and then used in computations of isochrones (Figure 2). First guess of the ellipse dimension is also based on estimations given by *Perissoratis and Papadopoulos* [1999]. The initial surface perturbation in the form of semiellipsoid with axes

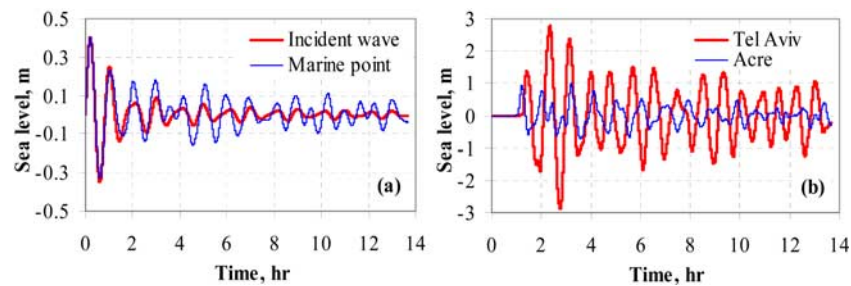


Figure 10. Numerically computed sea surface displacements excited by a “virtual wavemaker” located 400 km offshore: (a) incident wave and marigram at marine boundary point and (b) marigrams at Tel Aviv-Yafo and Acre nearshore points.

equal to the size of the landslide is used to compute tsunami wave parameters in the proximity to the Israeli coast.

4.2. Longwave Propagation Model

[39] The shallow-water theory is applied to simulate tsunami propagation. The considerable size of the area of interest requires an implementation of geographic coordinate system where the shallow water equations that account for the Coriolis force and bed friction are presented on a sphere. The computational algorithm used is based on a modification of the McCormack’s finite difference method to the solution of shallow water equations [Fedotova, 2006]. The model applied is essentially the same as described in the work of Chubarov and Fedotova [2003] and Shokin *et al.* [2006], and have been tested using benchmark problems given in the work of Yeh *et al.* [1996]. In particular, investigation of tsunami transformation [Shokin *et al.*, 2006] in a “washtub” model region enables the study of the peculiarities of different mathematical models and algorithms. It is aimed to reproduce the transformation of waves in regions with different depths and wave interaction with different types of boundaries (open and rigid reflecting boundaries). The bottom topography in the “washtub” region agrees well with the distribution of depths along the Kuril-Kamchatka Trough. The model has been verified by Shokin *et al.* [2006] via solution of two problems: The first is a one-dimensional describing propagation and reflection of a solitary wave within a basin of constant depth, and the second is two-dimensional, describing the transformation of initial perturbation of the free surface which is finite in both directions in plane. The importance of validation and verification of tsunami numerical models is stressed in the work of Synolakis *et al.* [2008]. According to these authors, this should be a continuous process and even proven models must be subjected to additional testing as new knowledge and data acquired. For more details regarding the shallow water equations, their finite difference presentation, and the numerical scheme, see Appendix A.

4.3. Numerical Modeling of Shelf Resonance

[40] In order to understand the nature of 50–60 min waves in the tide records, the numerical modeling is performed within the area that contains the eastern part of the Mediterranean basin stretching from $30^{\circ}30'E$ to $36^{\circ}30'E$ and from $31^{\circ}00'N$ to $37^{\circ}00'N$. A 15 s arc min grid resolution is used. The boundary condition at the western boundary is an incident wave envelope obtained by sum-

ming of sinusoidal waves with same amplitude and ranging from a 40- to 60-min period (time step is equal to 0.5 min), i.e., the input signal possesses 41 discrete frequencies that correspond to 40.0-, 40.5-, 41.0-, ..., 60.0-min periods without any initial phase lag. The marine boundary condition implies unlimited passage of the reflected waves outside the study domain. This process can be interpreted as a wavefield generation at the water surface within the basin by a “virtual wavemaker” placed at its far end, which is exciting in the water domain an initial perturbation with a wide bandwidth spectrum. A similar numerical study deal with evaluating the periods of free oscillations in basins with irregular geometry and bathymetry was recently presented in the work of Yalciner and Pelinovsky [2007].

[41] The analysis of modeling results is performed in the three selected locations: two coastal points (Tel Aviv ($32^{\circ}05'N$, $34^{\circ}45'E$) and Acre ($32^{\circ}55'N$, $35^{\circ}04'E$) and another location on the marine boundary ($33^{\circ}15'N$, $30^{\circ}30'E$)), where sea level oscillations represent a sum of incident and reflected waves. A marigram of the incident wave envelope and the resulted signal at the selected marine point are shown in Figure 10a, whereas the coastal marigrams are plotted in Figure 10b.

[42] Figure 11 shows spectra of coastal marigrams computed at Tel Aviv and Acre. At both locations the dominant harmonics fall into the time interval of 50–60 min (54 min for Tel Aviv and 58 min for Acre), as previously associated with regional phenomenon of shelf resonance (see section 3). Hence the numerical simulations performed confirm the presence of resonance on the Israeli continental shelf with frequencies in the 50- to 60-min range. Furthermore, we show in this section the model’s ability to represent adequately natural phenomena in the region of interest and thus may be considered as a verification of the numerical model developed in this study.

5. Modeling of the Historical 9 July 1956 Tsunami Triggered by an Earthquake in the Aegean Sea

[43] Simulations are performed from $30^{\circ}30'N$ to $38^{\circ}00'N$ and from $24^{\circ}00'E$ to $36^{\circ}00'E$. The specified boundary conditions ensure the free wave propagation through the open marine boundaries of the study domain and wave reflection from the coast boundary. Thirteen extraction points along the Israeli coast are selected for monitoring during the numerical simulation, but here the results are presented only in four: at Ashdod ($31^{\circ}49'N$, $34^{\circ}38'E$), Tel

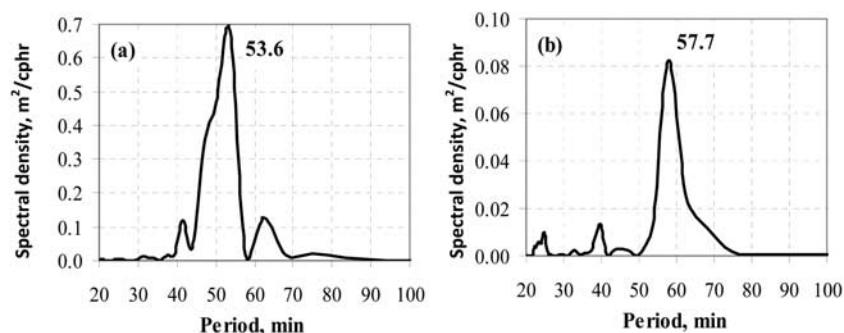


Figure 11. Smoothed spectra of the numerically computed sea surface displacement (see Figure 10b): at (a) Tel Aviv and (b) Acre.

Aviv (32°05'N, 34°45'E), Haifa (32°50'N, 34°59'E), and Acre (32°55'N, 35°04'E). The tsunami source is set using either a coseismic model of the source or by selecting initial perturbation suggested for landslide movement.

[44] The initial perturbation is placed at the epicenter for the coseismic tsunamigenic source (36°42'N, 25°48'E; see Figure 1) and is computed by applying the Gusiakov-Okada model [Gusiakov, 1978; Okada, 1985]. The fault parameters are determined from equations (1).

[45] Since the parameters of the 1956 earthquake as well as the correlation relations between earthquake and the initial perturbations that triggered the tsunami are somewhat ambiguous, we have chosen earthquake magnitude and its nonmagnitude-dependent geometrical characteristics in the range estimated from the geophysical studies [e.g., Ambraseys, 1960; Ambraseys and Jackson, 1990; Fritz et al., 2004; Okal et al., 2004; Perissoratis and Papadopoulos, 1999].

[46] In their paper dedicated to examination of seismicity of central Greece between 1890 and 1988, Ambraseys and Jackson [1990] suggest a fault with fault strike $\theta_0 = 60^\circ$; dip angle $\delta = 45^\circ$; and rake angle $\alpha = -90^\circ$ consistent with normal faulting on the steep escarpment along the SE coast of Amorgos Island, which bounds the deep Amorgos basin. Okal et al. [2004] used the preliminary determination of focal mechanisms (PDFM) method introduced by Reymond and Okal [2000] to invert a moment tensor from a limited set of spectral amplitudes of mantle waves. Their solution featured a normal faulting mechanism ($\theta_0 = 245^\circ$; $\delta = 67^\circ$; $\alpha = -79^\circ$) and a moment of 3.9×10^{27} dyn-cm⁻¹.

[47] We have also selected other rake and fault strike angles to generate maximum waves propagating toward the Israeli coast with varied the dip angle in a range to study its effect on the tsunami-wave characteristics. The considered events are listed in Table 3.

[48] In order to obtain reliable results, the selected grid should provide the necessary resolution of the numerical algorithm applied. For example, the marigrams obtained at four monitoring points along the coast for event 1 through utilizing different computational grids, 1-min and 15-s mesh, and plotted in Figure 12, and show that the features of the leading wave can be preserved even using a coarse grid. At all the points along the Israeli shore the numerically obtained amplitudes are in reasonable agreement with the records at the Yafu gauge (see Figures 4 and 6), i.e., ~ 15 cm (wave height ~ 30 cm). Nevertheless, qualitative and quantitative characteristics of the whole shallow water marigrams are strongly dependent on grid resolution. In our computations this impact is noticeable down to the grid resolution 15 s, i.e., the finer grid with 7.5-s mesh does not improve significantly the obtained results. Therefore, the 15-s grid with mesh is used within the coastal shallow water regions in the further simulations. Marigrams at Tel Aviv-Yafu for various tsunami events listed in Table 3 are presented in Figure 13. The depth of the coseismic source's focus does not noticeably affect the Tel Aviv marigram. Comparison between events 4 and 5, which share the same earthquake characteristics except the dip angle, indicates that the variation of this parameter affects moderately the wave amplitude. All considered sources yield amplitudes of oscillations that are closed to the measured values during the tsunami in 1956 (see Figure 13).

[49] No dominant maxima at ~ 15 -min frequencies as observed in the 1956 tsunami record can be found in the spectra of marigrams using the coseismic sources (see Figure 14, events 5 and 7). To examine other possibilities for generation of dominant spectral components close to the measured, it was assumed that this tsunami was excited by a landslide motion alone or by both coseismic and landslide sources. The process of landslide movement has not been

Table 3. Parameters of the Coseismic Tectonic Seabed Dislocation

Event	Earthquake Magnitude, M ()	Fault Length, L (km)	Fault Width, W (km)	Fault Depth, d_r (km)	Bottom Displacement, h_0 (m)	Dip Angle, δ (deg)	Rake Angle, α (deg)	Fault Strike, θ_0 (deg)
1	7.8	100	50	20	5.0	15	90	25
2	7.6	79.4	39.8	15	4.0	20	90	25
3	7.6	79.4	39.8	10	4.0	20	90	25
4	7.5	70.8	35.5	10	3.6	20	90	25
5	7.5	70.8	35.5	10	3.6	45	90	25
6	7.5	70.8	35.5	10	3.6	67	-79	245
7	7.5	70.8	35.5	10	3.6	45	-90	60

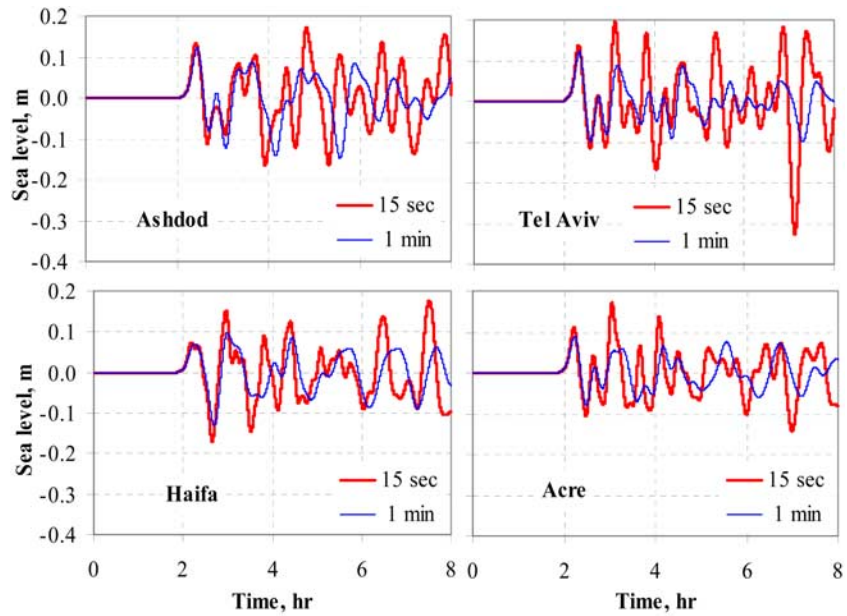


Figure 12. Numerically simulated sea surface elevations caused by a coseismic dislocation at the earthquake epicenter for coastal points at Ashdod, Tel Aviv, Haifa, and Acre. (See event 1 in Table 3.)

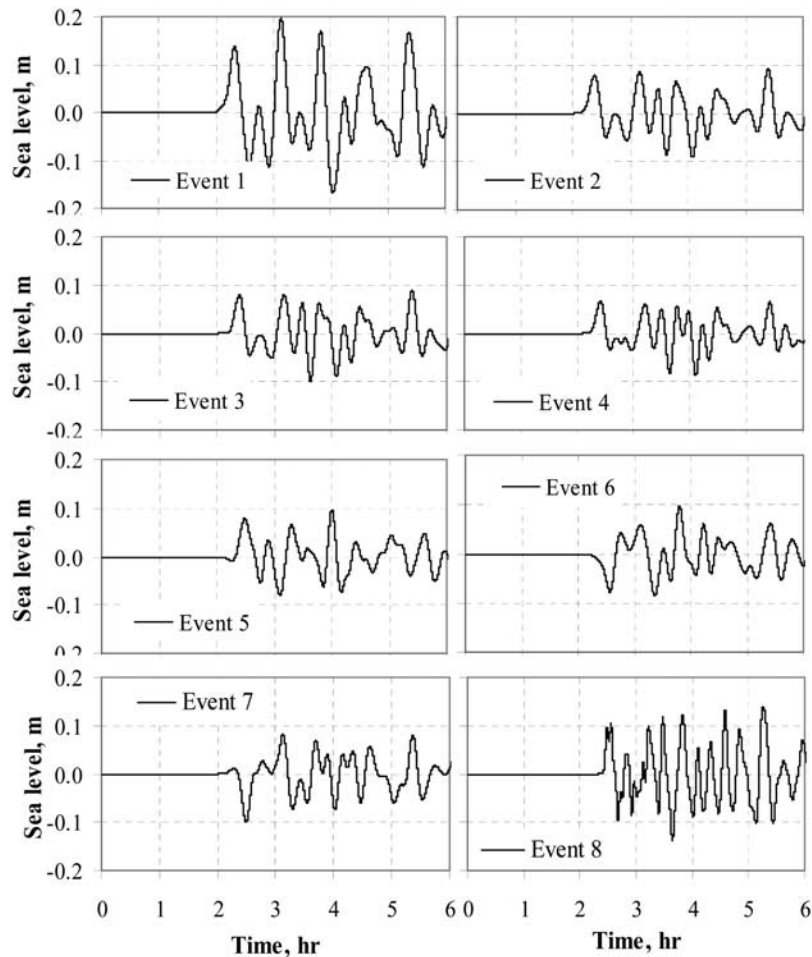


Figure 13. Computed marigrams at Tel Aviv-Yafo for various tsunami coseismic sources listed in Table 3 (events 1–7) and for the suggested initial disturbance of water surface due to a landslide triggered by an earthquake near the Amorgos trench (event 8).

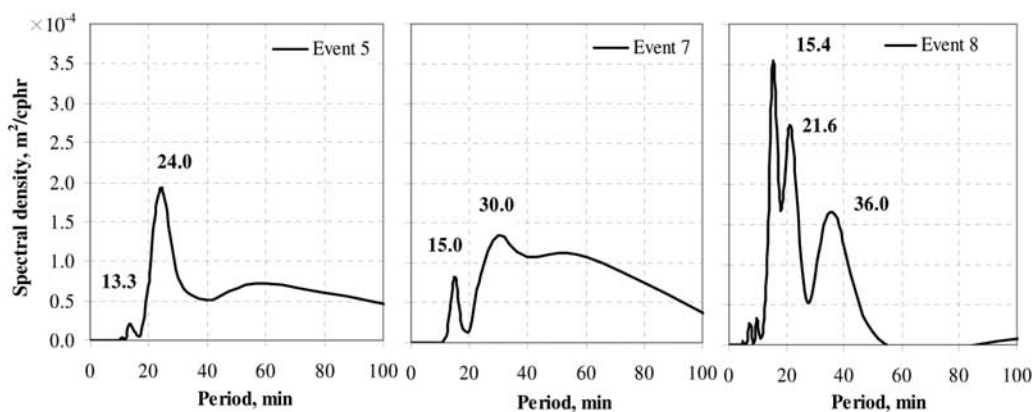


Figure 14. Smoothed spectra of the computed marigrams at Tel Aviv for tsunami coseismic sources (events 5 and 7 in Figure 13) and for the suggested initial disturbance of water surface due to a landslide (event 8 in Figure 13).

modeled in the framework of this study, though we estimated the ellipsoidal initial water surface disturbance on the basis of available information about this landslide. Both horizontal dimensions assumed to be of the same order of magnitude as the corresponding dimensions of the landslide assessed by *Perissoratis and Papadopoulos* [1999], i.e., ~ 20 km \times ~ 10 km. The initial wave height in the epicentral zone is approximated according to *Fritz et al.* [2004] and *Chubarov et al.* [2005]. *Fritz et al.* [2004] proposed the following empirical relationship:

$$\frac{\eta}{H} = 0.25 \left(\frac{v_s}{\sqrt{gH}} \right)^{1.4} \left(\frac{h_s}{H} \right)^{0.8}, \quad (3)$$

where H is the water depth; η is the maximum of initial wave height; v_s is the velocity of landslide movement; and h_s is the landslide thickness.

[50] The wave height η is estimated using equation (3) by changing the parameters in the range of water depth $H = 500$ – 720 m, velocity of landslide $v_s = 50$ – 80 m/s, and landslide thickness $h_s = 20$ – 50 m. For the above data, the maximum of initial wave height varies in the range $\eta = 10.0$ – 18.0 m. These values are in good agreement with the results of numerical modeling and laboratory experiments presented in the work of *Chubarov et al.* [2005]. The further computations are performed for $\eta = 15$ m. The initial perturbation having a shape of an ellipse is placed with its principal axis coinciding with the trough of the submarine trench of Amorgos as shown in Figure 2. Most of the wavefield computations are performed for a stationary initial perturbation. When the initial movement of the perturbation is assumed, the velocity of the flow is approximated in accordance with the longwave expression $u = \sqrt{g(H + \eta)} \cdot \eta / (H + \eta)$ and its direction may be varied.

[51] The marigram and spectrum of sea level oscillations computed for this initial perturbation (event 8) are shown in Figures 13 and 14 correspondingly. The dominating maximum of the resulted water fluctuations corresponds to the period ~ 15.5 min, which is very close to the main spectral constituent obtained for the level fluctuations measured at Yafu on 9 July 1956 (see Figure 7).

[52] Our main goal in the current study was to simulate the tsunami waves' oscillations in the far field recorded by

the Yafu tide gauge. The model used in this computation does not include an inundation module. Besides, the mareographs are located at the nearest to coast grid points with water depth at these points not less than 5 m. Nevertheless, in the following we present some comparisons between the observed runups at different islands within the Aegean Sea as given by *Ambraseys* [1960] and wave amplitudes computed in this near-field locations. It is obvious that such a model cannot provide meaningful wave heights for the location where wave runups above 5 m are observed. Therefore we limited our presentation to only those points where the observed runup heights are less than 5 m.

[53] The plots comparing the computed wave heights with the observed wave runups are presented in Figure 15 for perturbation with zero initial flow velocity and with velocity computed according to the above expression for long waves and its movement directed to the southeast. In spite of the very approximate shape of the chosen disturbance and the lack of inundation module in the model, the agreement is better than could be expected.

6. Conclusion

[54] The existing record of the 1956 Greek tsunami measured by tide gauge at the Yafu station has been digitized and analyzed. The computed spectra of high-frequency oscillations (the tidal components are eliminated) reveal the maximum energy constituent corresponding to 15-min period. These harmonics are also obtained numerically using a linear shallow water model for description of tsunami wave propagation with a properly selected tsunamigenic source.

[55] To exclude possible contamination of the resulting tsunami oscillations in the proximity to the Israeli coast by shelf resonance, the tidal records measured recently by the National Agency for Geodesy, Cadastre, Mapping and Geographic Information have been analyzed and compared to the results of special numerical study. In this study response to a wide spectrum of oscillations introduced at the sea boundary has been investigated. The obtained results are in a reasonable agreement with those obtained by the spectral analysis of the tidal records and thus provide clear

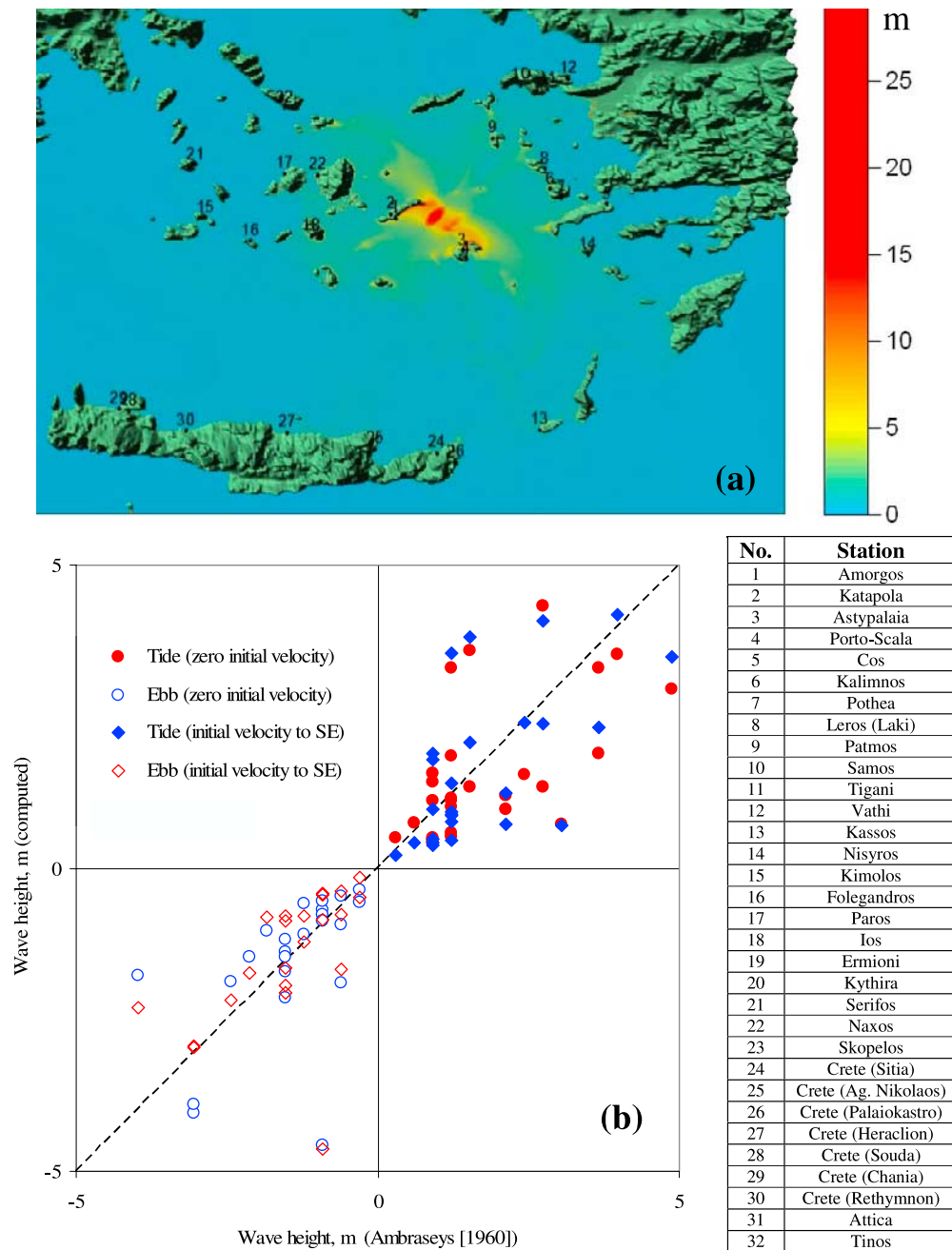


Figure 15. Tsunami waves simulations using the initial disturbance of water surface due to a landslide (initial perturbation has the ellipsoid shape): (a) near-field glow; and (b) comparison between the computed characteristics of the seismic sea waves of 9 July 1956 and those presented in the work of *Ambraseys* [1960]. Point numbering in Figure 15a corresponds to *Ambraseys* [1960] (see legend).

evidence of the presence of continental shelf resonance at time periods in the range of 50–60 min.

[56] Different coseismic tsunamigenic sources due to normal fault are evaluated and the tsunami wave propagation is investigated numerically. It appears that the selected model reproduces reasonably the wave height at the Tel Aviv-Yafo gauge station, but the spectra of computed mariograms in the proximity to the Israeli coast indicate that only small part of energy can be attributed to the spectral components with periods close to 15 min.

[57] On the basis of the comparison of the data related to 1956 Greek tsunami with the abundant literature and data on 1998 PNG, it was suggested that tsunami genesis could be attributed to two combined factors: the coseismic sea-floor displacement associated with the normal fault on the one hand and formation of a large sediment landslide caused by earthquake shock or/and aftershock on the other hand. Landslide dimensions have been guessed using limited geological information presented in existing publications and then have been assigned to the water surface distur-

bance in our numerical modeling of the tsunami excited by the landslide movement. As a result, the spectra of the computed numerically marigrams contain the major energetic spectral components with periods close to the recorded 15 min, which confirms the landslide nature of the tsunami-migenic source responsible for generation of these high-frequency (relatively to astronomic tide constituents) energy components in the spectrum.

[58] Comparisons between the observed runups at different islands within the Aegean Sea as given in the work of *Ambraseys* [1960] and wave amplitudes computed in this study within the near-field locations have been performed. In spite of the very approximate shape of the chosen disturbance and the lack of inundation module in the model, the agreement is better than could be expected.

Appendix A

[59] The mathematical model applied for the numerical simulations is the shallow water system

$$\begin{aligned} \frac{\partial h}{\partial t} + \frac{1}{R \cos \varphi} \left[\frac{\partial hu}{\partial \lambda} + \frac{\partial hv \cos \varphi}{\partial \varphi} \right] &= 0, \\ \frac{\partial u}{\partial t} + \frac{1}{R} \left[\frac{1}{2 \cos \varphi} \frac{\partial u^2}{\partial \lambda} + v \frac{\partial u}{\partial \varphi} + \frac{g}{\cos \varphi} \frac{\partial \eta}{\partial \lambda} \right] &= f_1, \\ \frac{\partial v}{\partial t} + \frac{1}{R} \left[\frac{u}{\cos \varphi} \frac{\partial v}{\partial \lambda} + \frac{1}{2} \frac{\partial v^2}{\partial \varphi} + g \frac{\partial \eta}{\partial \varphi} \right] &= f_2. \end{aligned} \quad (\text{A1})$$

where R is the average Earth's radius; λ and φ are the geographic longitude and latitude, respectively; t is the time; $h = H + \eta$ is the total depth with H being the thickness of the undisturbed water body and η is the free surface displacement; g is the acceleration of gravity; u and v are the components of the depth-averaged velocity vector in λ and φ directions, respectively. In equation (A1) the values of f_1 and f_2 are given by

$$f_1 = lv - gk^2 \frac{u\sqrt{u^2 + v^2}}{h^{4/3}}, \quad f_2 = -lu - gk^2 \frac{v\sqrt{u^2 + v^2}}{h^{4/3}}, \quad (\text{A2})$$

where k is the roughness coefficient and $l = 2\omega \sin \varphi$ with ω denoting the angular velocity of Earth's rotation.

[60] An even rectangular grid in the plane of geographic coordinates λ and φ

$$\bar{\Omega} = \left\{ (\lambda_i, \varphi_j) : \underline{\lambda} \leq \lambda_i \leq \bar{\lambda}, \underline{\varphi} \leq \varphi_j \leq \bar{\varphi}, 0 \leq i \leq N_\lambda, 0 \leq j \leq N_\varphi \right\}$$

with the corresponding spatial increments of $\Delta\lambda$ and $\Delta\varphi$, is introduced within the study area

$$\Omega(\lambda, \varphi) = \left\{ (\lambda, \varphi) : \underline{\lambda} \leq \lambda \leq \bar{\lambda}, \underline{\varphi} \leq \varphi \leq \bar{\varphi}, \underline{\lambda}, \underline{\varphi}, \bar{\lambda}, \bar{\varphi} - \text{const} \right\}.$$

The time increment at the step n is $\Delta\tau^n = t^{n+1} - t^n$. In terms of mesh functions related to the discrete variables $\lambda_i, \varphi_j, t^n$, an explicit double-step finite difference McCormack's scheme adopted for linear model approximation (A1) in inner points of the grid $\bar{\Omega}$ is as follows:

[61] The first step is

$$\begin{aligned} \frac{\hat{h}_{ij} - h_{ij}^n}{\tau^n} + \frac{1}{R \cos \varphi_j} & \cdot \left[\frac{h_{ij}^n u_{ij}^n - h_{i-1j}^n u_{i-1j}^n}{\Delta\lambda} + \frac{\cos \varphi_j h_{ij}^n v_{ij}^n - \cos \varphi_{j-1} h_{ij-1}^n v_{ij-1}^n}{\Delta\varphi} \right] = 0, \\ \frac{\hat{u}_{ij} - u_{ij}^n}{\tau^n} + \frac{1}{R \cos \varphi_j} & \left[\frac{(u_{ij}^n)^2 - (u_{i-1j}^n)^2}{2\Delta\lambda} + g \frac{\eta_{ij}^n - \eta_{i-1j}^n}{\Delta\lambda} \right] \\ & + \frac{v_{ij}^n u_{ij}^n - u_{ij-1}^n u_{ij}^n}{R \Delta\varphi} = f_{1j}^n, \\ \frac{\hat{v}_{ij} - v_{ij}^n}{\tau^n} + \frac{u_{ij}^n v_{ij}^n - v_{i-1j}^n v_{ij}^n}{R \cos \varphi_j \Delta\lambda} & + \frac{1}{R} \left[\frac{(v_{ij}^n)^2 - (v_{ij-1}^n)^2}{2\Delta\varphi} + g \frac{\eta_{ij}^n - \eta_{ij-1}^n}{\Delta\varphi} \right] = f_{2j}^n. \end{aligned} \quad (\text{A3})$$

where

$$f_{1j}^n = l_j v_{ij}^n - gk^2 \frac{u_{ij}^n \sqrt{(u_{ij}^n)^2 + (v_{ij}^n)^2}}{(h_{ij}^n)^{4/3}}$$

$$f_{2j}^n = -l_j u_{ij}^n - gk^2 \frac{v_{ij}^n \sqrt{(u_{ij}^n)^2 + (v_{ij}^n)^2}}{(h_{ij}^n)^{4/3}}$$

with $l_j = 2\omega \sin \varphi_j$.

[62] The second step is

$$\begin{aligned} \frac{h_{ij}^{n+1} - (h_{ij}^n + \hat{h}_{ij})/2}{\tau^n/2} + \frac{1}{R \cos \varphi_j} & \left[\frac{\hat{h}_{i+1j} \hat{u}_{i+1j} - \hat{h}_{ij} \hat{u}_{ij}}{\Delta\lambda} + \frac{\cos \varphi_{j+1} \hat{h}_{ij+1} \hat{v}_{ij+1} - \cos \varphi_j \hat{h}_{ij} \hat{v}_{ij}}{\Delta\varphi} \right] = 0, \\ \frac{u_{ij}^{n+1} - (u_{ij}^n + \hat{u}_{ij})/2}{\tau^n/2} + \frac{1}{R \cos \varphi_j} & \left[\frac{(\hat{u}_{i+1j})^2 - (\hat{u}_{ij})^2}{2\Delta\lambda} + g \frac{\hat{h}_{i+1j} - H_{i+1j}^n - \hat{h}_{ij} + H_{ij}^n}{\Delta\lambda} \right] + \frac{\hat{v}_{ij} \hat{u}_{ij+1} - \hat{u}_{ij} \hat{v}_{ij}}{R \Delta\varphi} = \hat{f}_{1j}, \\ \frac{v_{ij}^{n+1} - (v_{ij}^n + \hat{v}_{ij})/2}{\tau^n/2} + \frac{\hat{u}_{ij}}{R \cos \varphi_j} & \frac{\hat{v}_{i+1j} - \hat{v}_{ij}}{\Delta\lambda} + \frac{1}{R} \left[\frac{(\hat{v}_{ij+1})^2 - (\hat{v}_{ij})^2}{2\Delta\varphi} + g \frac{\hat{h}_{ij+1} - H_{ij+1}^n - \hat{h}_{ij} + H_{ij}^n}{\Delta\varphi} \right] = \hat{f}_{2j}. \end{aligned} \quad (\text{A4})$$

where

$$\hat{f}_{1_{ij}} = l_j \hat{v}_{ij} - gk^2 \frac{\hat{u}_{ij} \sqrt{(\hat{u}_{ij})^2 + (\hat{v}_{ij})^2}}{(\hat{h}_{ij})^{4/3}}$$

$$\hat{f}_{2_{ij}} = -l_j \hat{u}_{ij}^n - gk^2 \frac{\hat{v}_{ij}^n \sqrt{(\hat{u}_{ij}^n)^2 + (\hat{v}_{ij}^n)^2}}{(\hat{h}_{ij})^{4/3}}.$$

[63] The upper and lower boundaries of the study domain are parallel to the Equator, while the left and the right boundaries are placed along the meridians. For reflecting inner boundaries the “upper” and the “lower” boundary conditions are $v=0$, $\partial u/\partial \varphi=0$, $\partial \eta/\partial \varphi=0$, whereas the “left” and the “right” boundary conditions are $u=0$, $\partial v/\partial \lambda=0$, $\partial \eta/\partial \lambda=0$. Free wave propagation through the open external boundaries of the study domain $\Omega(\lambda, \varphi)$ is specified (Sommerfeld’s conditions), which in the selected coordinate system are given on the upper and lower boundaries by

$$R \frac{\partial \eta}{\partial t} \pm c \frac{\partial \eta}{\partial \varphi} = 0, \quad R \frac{\partial u}{\partial t} \pm c \frac{\partial u}{\partial \varphi} = 0, \quad R \frac{\partial v}{\partial t} \pm c \frac{\partial v}{\partial \varphi} = 0, \quad (\text{A5})$$

and on the left and right boundaries by

$$R \frac{\partial \eta}{\partial t} \pm \frac{c}{\cos \varphi} \frac{\partial \eta}{\partial \lambda} = 0, \quad R \frac{\partial u}{\partial t} \pm \frac{c}{\cos \varphi} \frac{\partial u}{\partial \lambda} = 0,$$

$$R \frac{\partial v}{\partial t} \pm \frac{c}{\cos \varphi} \frac{\partial v}{\partial \lambda} = 0, \quad (\text{A6})$$

where $c = \sqrt{gh}$ is the wave celerity with sign depending on the orientation of the boundary normal.

Notation

c	wave celerity, m/s.
d_f	fault depth, m.
g	acceleration of gravity, m/s^2 .
H	seawater depth, m.
h	total depth, m.
h_0	bottom displacement, m.
h_s	slump thickness, m.
k	roughness coefficient.
L	fault length, km.
l	shelf width, km.
M	earthquake magnitude.
n	number of time step.
R	average Earth’s radius, km.
s	continental shelf slope.
T	period of the dominated mode in a resonant system, min.
t	time, s.
u	component of the depth-averaged velocity vector in λ direction, m/s.
v	component of the depth-averaged velocity vector in φ direction, m/s.
v_s	velocity of landslide movement, m/s.
W	fault width, km.

α	rake angle, degrees.
δ	dip angle, degrees.
η	free surface displacement, m.
θ_0	fault azimuth, degrees.
λ	geographic longitude, degrees.
$\Delta \lambda$	spatial increment in λ direction, degrees.
φ	geographic latitude, degrees.
$\Delta \varphi$	spatial increment in φ direction, degrees.
ω	angular velocity of Earth’s rotation, s^{-1} .
$\Omega(\lambda, \varphi)$	study area.
$\Delta \tau^n$	time increment at the step n , s.

[64] **Acknowledgments.** The current work is carried out in the framework of Israeli-Russian joint research supported by Ministry of Science and Technology project 05414151; the State of Israel; and Russian Foundation for Basic Research projects 06-05-64869, 06-05-72011, 06-05-72014, 07-05-13583, 08-02-00039, 08-05-00069, and 09-05-91222. The generous financial help of Program of Fundamental International Research SB RAS projects 28 and 113; the Program of Government Support of Scientific Research conducted by leading scientific schools of the Russian Federation 931.2008.9; and projects INTAS 06-1000013-9236 is greatly appreciated. The work is supported in part by Israel Science Foundation grant 964/05. The authors are very grateful to the National Mapping Agency for providing the required seawater level database in Ashdod, Tel Aviv, and Acre. Personal thanks must also be expressed to Amotz Agnon for his generous help providing important information about the Mediterranean Sea region potential seismology and about the 9 July 1956 tsunami generation source.

References

- Ambraseys, N. N. (1960), The seismic sea wave of July 9, 1956, in the Greek Archipelago, *J. Geophys. Res.*, *65*, 1257–1265, doi:10.1029/JZ065i004p01257.
- Ambraseys, N. (2008), *Earthquakes in the Eastern Mediterranean and the Middle East: A Multidisciplinary Study of 2000 Years of Seismicity*, Cambridge Univ. Press, New York.
- Ambraseys, N. N., and J. A. Jackson (1990), Seismicity and associated strain of central Greece between 1890 and 1988, *Geophys. J. Int.*, *101*, 663–708, doi:10.1111/j.1365-246X.1990.tb05577.x.
- Amiran, D. H., K. E. Arieh, and T. Turcotte (1994), Earthquakes in Israel and adjacent areas: Macroseismic observations since 100 B.C.E., *Isr. Explor. J.*, *44*, 260–305.
- Camilleri, D. H. (2006), Tsunami construction risks in the Mediterranean—Outlining Malta’s scenario, *Disaster Prev. Manage.*, *15*(1), 146–162, doi:10.1108/09653560610654301.
- Chubarov, L. B., and Z. I. Fedotova (2003), An effective high accuracy method for tsunami run-up numerical modeling, in *Submarine Landslides and Tsunamis*, NATO Sci. Ser., vol. IV, *Earth and Environmental Sciences*, edited by C. Ahmet et al., pp. 203–216, Kluwer Acad., Norwell, Mass.
- Chubarov, L. B., S. V. Eletsii, Z. I. Fedotova, and G. S. Khakimzyanov (2005), Simulation of surface waves generation by an underground landslide, *Russ. J. Numer. Anal. Math. Model.*, *20*(5), 425–437, doi:10.1515/156939805775186668.
- Dutykh, D., F. Dias, and Y. Kervella (2006), Linear Theory of wave generation by a moving bottom, *C. R. Acad. Sci., Ser. I.*, *343*, 499–504.
- Emery, W. J., and R. E. Thomson (1997), *Data Analysis Methods in Physical Oceanography*, Pergamon, New York.
- Fedotova, Z. I. (2006), On the using of MacCormack finite-difference scheme in wave hydrodynamic problems (in Russian), *Comput. Technol.*, *11*, 53–63.
- Fritz, H. M., W. H. Hager, and H.-E. Minor (2004), Near field characteristics of landslide generated impulse waves, *J. Waterw. Port Coastal Ocean Eng.*, *130*, 287–302.
- Galton-Fenzi, B. K., W. D. Scott, D. E. Farrow, and R. Handsworth (2006), Revisiting the anomalous shelf water oscillations of Buckles Bay, Macquarie Island, *Cont. Shelf Res.*, *26*(19), 2386–2392, doi:10.1016/j.csr.2006.07.010.
- Gelfenbaum, G., and B. Jaffe (2003), Erosion and sedimentation from the 17 July, 1998, Papua New Guinea tsunami, *Pure Appl. Geophys.*, *160*, 1969–1999, doi:10.1007/s00024-003-2416-y.
- Goldsmith, V., and M. Gilboa (1986), Tide and low in Israel (in Hebrew), *Ofakim Be’Geographia*, *15*, 21–47.
- Guidoboni, E., and A. Comastri (1997), The large earthquake of 8 August 1303 in Crete: Seismic scenario and tsunami in the Mediterranean area, *J. Seismol.*, *1*(1), 55–72, doi:10.1023/A:1009737632542.

- Gusiakov, V. K. (1978), Residual displacements on the surface of elastic half-space, in *Conditionally Correct Problems of Mathematical Physics in Interpretation of Geophysical Observations* (in Russian), pp. 23–51, Comput. Cent., Russ. Acad. of Sci., Novosibirsk, Russia.
- Harbitz, C. B., F. Løvholt, G. Pedersen, and D. G. Masson (2006), Mechanisms of tsunami generation by submarine landslides: A short review, *Norw. J. Geol.*, *86*, 255–264.
- Japan Meteorological Agency (JMA) (2001), *Handbook for Tsunami Forecast in the Japan Sea*, Tokyo.
- Kawata, Y., B. C. Benson, J. Borrero, H. Davies, W. de Lange, F. Imamura, and C. E. Synolakis (1999), Tsunami in Papua New Guinea, *Eos Trans. AGU*, *80*(9), 101–105, doi:10.1029/99EO00065.
- Kervella, Y., D. Dutykh, and F. Dias (2007), Comparison between three-dimensional linear and nonlinear tsunami generation models, *Theor. Comput. Fluid Dyn.*, *21*, 245–269, doi:10.1007/s00162-007-0047-0.
- Lynett, P. J., J. C. Borrero, P. L. F. Liu, and C. E. Synolakis (2003), Field survey and numerical simulations: A review of the 1998 Papua New Guinea tsunami, *Pure Appl. Geophys.*, *160*, 2119–2146, doi:10.1007/s00024-003-2422-0.
- Matsumoto, T., D. R. Tappin, and the SOS Onboard Scientific Party (2003), Possible coseismic large-scale landslide off the northern coast of Papua New Guinea in July 1998: Geophysical and geological results from SOS cruises, *Pure Appl. Geophys.*, *160*, 1923–1943, doi:10.1007/s00024-003-2414-0.
- Munk, W. H. (1962), Long ocean waves, in *The Sea: Ideas and Observations in Progress in Study of the Sea*, edited by M. N. Hill, pp. 647–664, Wiley-Interscience, Hoboken, N. J.
- Okada, Y. (1985), Surface deformation due to shear and tensile faults in the half-space, *Bull. Seismol. Soc. Am.*, *75*, 1135–1154.
- Okal, E. A. (2003a), T waves from the 1998 Papua New Guinea earthquake and its aftershocks: Timing the tsunamigenic slump, *Pure Appl. Geophys.*, *160*, 1843–1863, doi:10.1007/s00024-003-2409-x.
- Okal, E. A. (2003b), Normal mode energetics for far-field tsunamis generated by dislocations and landslides, *Pure Appl. Geophys.*, *160*, 2189–2221, doi:10.1007/s00024-003-2426-9.
- Okal, E. A., and C. E. Synolakis (2004), Source discriminants for near-field tsunamis, *Geophys. J. Int.*, *158*, 899–912, doi:10.1111/j.1365-246X.2004.02347.x.
- Okal, E. A., C. E. Synolakis, and A. C. Yalciner (2004), The Amorgos, Greece, earthquake and tsunami of 9 July 1956: Focal mechanism and field survey, *Eos Trans. AGU*, *85*(47), Fall Meet. Suppl., Abstract OS23D-1358.
- Okal, E. A., C. E. Synolakis, B. Uslu, N. Kalligeris, and E. Voukouvalas (2009), The 1956 earthquake and tsunami in Amorgos, Greece, *Geophys. J. Int.*, in press.
- Pattiaratchi, C. B., and E. M. S. Wijeratne (2009), Tide gauge observations of 2004–2007 Indian Ocean tsunamis from Sri Lanka and Western Australia, *Pure Appl. Geophys.*, *166*, 233–258, doi:10.1007/s00024-008-0434-5.
- Pelinovsky, E., B. H. Choi, A. Stromkov, I. Didenkulova, and H. S. Kim (2005), Analysis of tide-gauge records of the 1883 Krakatau tsunami, in *Tsunamis: Case Studies and Recent Developments*, edited by K. Satake, pp. 57–78, Springer, New York.
- Perissoratis, C., and G. A. Papadopoulos (1999), Sediment instability and slumping in the southern Aegean Sea and the case history of the 1956 tsunami, *Mar. Geol.*, *161*, 287–305, doi:10.1016/S0025-3227(99)00039-0.
- Reinhardt, E. G., B. N. Goodman, J. I. Boyce, G. Lopez, P. van Hengstum, W. J. Rink, Y. Mart, and A. Raban (2006), The tsunami of December 13, 115 A.D. and the destruction of Herod the Great's Harbour at Caesarea Maritima, Israel, *Geology*, *34*, 1061–1064, doi:10.1130/G22780A.1.
- Reymond, D., and E. A. Okal (2000), Preliminary determination of focal mechanisms from the inversion of spectral amplitudes of mantle waves, *Phys. Earth Planet. Inter.*, *121*, 249–271, doi:10.1016/S0031-9201(00)00171-0.
- Salamon, A., T. Rockwell, and S. Ward (2007), Tsunami hazard evaluation of the eastern Mediterranean: Historical analysis and selected modeling, *Bull. Seismol. Soc. Am.*, *97*(3), 705–724, doi:10.1785/0120060147.
- Shokin, Y. I., L. B. Chubarov, Z. I. Fedotova, S. A. Beizel, and S. V. Eletsky (2006), Principles of numerical modeling applied to the tsunami problem, *Russ. J. Earth Sci.*, *8*, ES6004, doi:10.2205/2006ES000216.
- Soloviev, S. L., O. N. Solovieva, C. N. Go, K. S. Kim, and N. A. Shchetnikov (Eds.) (2000), *Tsunamis in the Mediterranean Sea 2000 B.C.–2000 A.D., Advances in Natural and Technological Hazards Research*, vol. 13, Springer, New York.
- Stiros, S. C., L. Marangou, and M. Arnold (1994), Quaternary uplift and tilting of Amorgos Island (southern Aegean) and the 1956 earthquake, *Earth Planet. Sci. Lett.*, *128*, 65–76, doi:10.1016/0012-821X(94)90135-X.
- Synolakis, C. E., and E. N. Bernard (2006), Tsunami science before and beyond Boxing Day 2004, *Philos. Trans. R. Soc. A*, *364*, 2231–2265, doi:10.1098/rsta.2006.1824.
- Synolakis, C. E., and E. A. Okal (2005), 1992–2002: Perspective on a decade of post tsunami surveys, *Adv. Nat. Technol. Hazards*, *23*, 1–29, doi:10.1007/1-4020-3331-1_1.
- Synolakis, C. E., J. P. Bardeř, J. C. Borrero, H. L. Davies, E. A. Okal, E. A. Silver, S. Sweet, and D. R. Tappin (2002), The slump origin of the 1998 Papua New Guinea tsunami, *Proc. R. Soc. London, Ser. A*, *458*, 763–789, doi:10.1098/rspa.2001.0915.
- Synolakis, C. E., E. N. Bernard, V. V. Titov, U. Kanoglu, and F. I. Gonzalez (2008), Validation and verification of tsunami numerical models, *Pure Appl. Geophys.*, *165*, 2197–2228, doi:10.1007/s00024-004-0427-y.
- Tappin, D. R., P. Watts, G. M. McMurtry, Y. Lafoy, and T. Matsumoto (2001), The Sissano, Papua New Guinea, tsunami of July 1998—Offshore evidence on the source mechanism, *Mar. Geol.*, *175*, 1–23, doi:10.1016/S0025-3227(01)00131-1.
- Tappin, D. R., P. Watts, and S. T. Grilli (2008), The Papua New Guinea tsunami of 17 July 1998: Anatomy of a catastrophic event, *Nat. Hazards Earth Syst. Sci.*, *8*, 243–266.
- Van Dorn, W. G. (1987), Tide gage response to tsunami. part II: Other oceans and smaller seas, *J. Phys. Oceanogr.*, *17*, 1507–1516, doi:10.1175/1520-0485(1987)017<1507:TGRTP>2.0.CO;2.
- Wells, D. L., and K. J. Coppersmith (1994), New empirical relationships among magnitude, rupture length, rupture width, rupture area, and surface displacement, *Bull. Seismol. Soc. Am.*, *84*(4), 974–1002.
- Yalciner, A. C., and E. N. Pelinovsky (2007), A short cut numerical method for determination of periods of free oscillations for basins with irregular geometry and bathymetry, *Ocean Eng.*, *34*, 747–757, doi:10.1016/j.oceaneng.2006.05.016.
- Yanuma, T., and Y. Tsui (1998), Observation of edge waves trapped on the continental shelf in the vicinity of Makurazaki Harbor, Kyushu, Japan, *J. Oceanogr.*, *54*, 9–18, doi:10.1007/BF02744377.
- Yeh, H., P. L. F. Liu, and C. E. Synolakis (Eds.) (1996), *Long-Wave Runup Models*, World Sci., Tokyo.

S. Beisel, L. Chubarov, and Y. Shokin, Institute of Computational Technologies, Siberian Branch of the Russian Academy of Sciences, 6 Lavrentiev Avenue, Novosibirsk 630090, Russia.

I. Didenkulova, Department of Mechanics and Applied Mathematics, Institute of Cybernetics, Tallinn University of Technology, Tallinn 12618, Estonia.

E. Kit, School of Mechanical Engineering, Faculty of Engineering, Tel Aviv University, Tel Aviv 69978, Israel. (kit@eng.tau.ac.il)

A. Levin and M. Sladkevich, Coastal and Marine Engineering Research Institute, Technion City, Haifa 32000, Israel.

E. Pelinovsky, Department of Nonlinear Geophysical Processes, Institute of Applied Physics, Russian Academy of Sciences, 46 Uljanov Street, Nizhny Novgorod 603950, Russia.